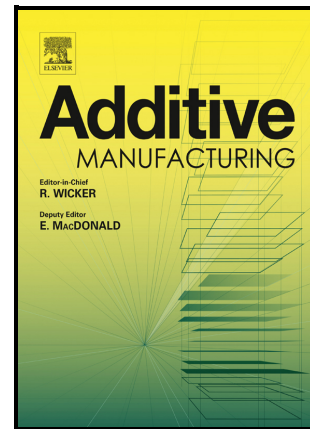


The effects of powder reuse on the mechanical response of electron beam additively manufactured Ti6Al4V parts

Gowtham Soundarapandiyan, Carol Johnston, Raja H.U. Khan, Chu Lun Alex Leung, Peter D. Lee, Everth Hernández-Nava, Bo Chen, Michael E. Fitzpatrick



PII: S2214-8604(21)00266-9

DOI: <https://doi.org/10.1016/j.addma.2021.102101>

Reference: ADDMA102101

To appear in: *Additive Manufacturing*

Received date: 8 October 2020

Revised date: 26 March 2021

Accepted date: 3 June 2021

Please cite this article as: Gowtham Soundarapandiyan, Carol Johnston, Raja H.U. Khan, Chu Lun Alex Leung, Peter D. Lee, Everth Hernández-Nava, Bo Chen and Michael E. Fitzpatrick, The effects of powder reuse on the mechanical response of electron beam additively manufactured Ti6Al4V parts, *Additive Manufacturing*, (2020) doi:<https://doi.org/10.1016/j.addma.2021.102101>

This is a PDF file of an article that has undergone enhancements after acceptance, such as the addition of a cover page and metadata, and formatting for readability, but it is not yet the definitive version of record. This version will undergo additional copyediting, typesetting and review before it is published in its final form, but we are providing this version to give early visibility of the article. Please note that, during the production process, errors may be discovered which could affect the content, and all legal disclaimers that apply to the journal pertain.

The effects of powder reuse on the mechanical response of electron beam additively manufactured Ti6Al4V parts

Gowtham Soundarapandiyar^{1,3,*}, Carol Johnston², Raja H.U. Khan², Chu Lun Alex Leung^{4,5}, Peter D. Lee^{4,5}, Everth Hernández-Nava⁷, Bo Chen^{3,6}, Michael E. Fitzpatrick³

¹National Structural Integrity Research Centre (NSIRC), Granta Park, Cambridge, CB21 6AL, UK

²TWI Ltd, Granta Park, Cambridge, CB21 6AL, UK

³Faculty of Engineering, Environment and Computing, Coventry University, Coventry, CV1 5FB, UK

⁴Department of Mechanical Engineering, University College London, WC1E 7JE, UK

⁵Research Complex at Harwell, Rutherford Appleton Laboratory, Harwell, Didcot, OX11 0FA, UK

⁶School of Engineering, University of Leicester, Leicester, LE1 7RH, UK

⁷The University of Sheffield, Materials Science and Engineering, Sir Robert Hadfield building, Sheffield, UK

*Corresponding author: e-mail: soundarg@uni.coventry.ac.uk

Abstract

High cost of metal powders has increased the demand for recycling of unmelted powder in electron beam powder bed fusion additive manufacturing process. However, powder characteristics are likely to change during manufacturing, recovery and reuse. It is important to track the evolution of powder characteristics at different stages of recycling to produce components with consistent properties. The present work evaluates the changes in Ti6Al4V powder properties during manufacturing by characterising powder particles at different locations in the powder bed; recovery and reuse, through evaluating the effects of the powder recovery system and sieving for 10 build cycles. Heterogeneous powder degradation occurred during manufacturing with the particles closer to the melt zone showing higher oxygen content and thicker α laths with β phase boundaries. Most of them had a hard-sintered and agglomerated powder morphology in contrast to particles at the edges of the powder bed. Recovery and reuse resulted in a refined particle size distribution, but only marginal change in powder morphology. The increased oxygen caused a slight increase in the yield and tensile strengths of the build. The effect of powder reuse on material elongation, hardness and Charpy impact energy was negligible. The high cycle fatigue performance deteriorated with reuse due to the increased lack-of-fusion defects. This might be attributed to the voids formed in the powder bed due to decrease in the number of fine particles coupled with an increase in the number of high-aspect ratio particles.

Keywords: Additive manufacturing, Electron beam powder bed fusion, Powder reuse, Powder characteristics, Build properties

1. Introduction

Electron-beam powder bed fusion (EB-PBF) technology is one of the prominent layer-by-layer additive manufacturing (AM) techniques widely used to produce near-net shaped components for aerospace, dental, energy and automotive industries [1,2]. In EB-PBF system, an electron beam is used to melt and fuse metal powder selectively to produce the desired component. The process has several advantages such as less material wastage, shorter lead time, excellent buy-to-fly ratio etc. [3]. EB-PBF process involves powder raking, preheating, melting, post-heating, followed by powder and part recovery. Powder spreading involves the deposition of a thin powder layer over the build platform by a raking mechanism followed by a preheating process, which is performed in two stages commonly referred to as preheat 1 and preheat 2 [4,5]. Preheat 1 is applied to the entire build area, whereas preheat 2 is applied only over the area which will be melted. A defocused electron beam is used at high scanning speed so that the energy input is low enough to sinter the powder particles. This is performed to avoid charging of the powder by electrons, commonly referred to as ‘powder smoke’ [6], and to reduce residual stress development in the part caused by rapid cooling [7]. Following preheating, selective melting is performed using a focused electron beam at relatively low scanning speed. After melting, post-heating is performed over the entire build area, to normalise the powder bed temperature gradient for the next layer [8]. The build platform, then descends by a distance corresponding to the layer height, a fresh layer of powder is spread and the process continues.

Once the fabrication is completed, the unconsumed powder is generally recovered and recycled to improve the process efficiency [9]. Some of the powder particles in the recycled condition are likely to be affected during the manufacturing process or during powder handling while recycling. Consequently, the recycled powder will not have the same physical and chemical properties as the virgin powder [10,11]. Ensuring the quality of recycled powder is one of the key parameters to maintain consistency in build properties [12–14]. Recently, several industries and government agencies are focusing on the development of standards and qualification of AM powder feedstock to establish a feedstock-parameter-structure-properties relationship. Therefore, it is critical to understand the evolution of powder characteristics with recycling, and the potential degradation mechanisms of the powder feedstock. Changes in powder intrinsic and extrinsic properties with recycling depend on several factors such as alloy type, chemical composition, component geometry, processing parameters, recycling method etc.

Research has been performed to understand the effects of recycling on powder and part properties in different materials such as IN718 [15–19], AlSi10Mg [17,20], Ti6Al4V [13,17,18,21–27] and 316L austenitic steel [12] in both the EB-PBF and laser powder-bed fusion (L-PBF) processes. In EB-PBF, Gruber *et al.* [19] reported changes in the surface chemistry of the IN718 powder particles after multiple reuses. A heterogeneous oxide layer with Al-rich particulates was observed in the recycled powder, which increased with recycling due to the selective oxidation of Al present on the powder surface. In addition, morphological changes such as an increase in the fraction of coarser particles, satellites, and agglomerates have also been observed in both L-PBF [17] and EB-PBF [18]. In highly reactive alloys like Ti6Al4V, there is a progressive increase in the powder O content caused by the exposure of the powder surface to humidity in the environment during powder handling [24].

Among the many studies of recyclability in powder-bed AM processes, Ti6Al4V is one of the most widely investigated alloys, due to its wide range of potential applications. However, there are still shortcomings in the previous studies that need to be explored such as:

- (i) Evolution of powder microstructure.
- (ii) Changes in powder characteristics with respect to different locations in the powder bed.
- (iii) Effects of powder recycling on defect population and size distribution.
- (iv) Compared to the plasma-atomised powders, little attention has been given to gas-atomised ones in terms of the powder reuse EB-PBF work.

To help fill in the research gap, the properties of argon-gas-atomised (AGA) Ti6Al4V powders in the EB-PBF process was investigated, with respect to locations in the powder bed and the number of reuse times. The powders were characterised using a range of techniques. The microstructure and mechanical properties of EB-PBF Ti6Al4V specimens fabricated using both virgin and recycled powders were also investigated.

2. Experimental Methodology

2.1 Material and approach

The work was conducted in an ARCAM Q10 plus EB-PBF system using 35 kg of AGA Ti6Al4V extra-low-interstitial (ELI) powder supplied by Carpenter Additive, UK. A

controlled and simulated recycling methodology was employed to reduce top-up with virgin powder, reduce powder consumption and to maintain consistency in the build volume. Figure 1 shows the manufacturing strategy adopted in this work. Virgin condition corresponds to manufacturing of four test coupons of the same geometry ($120 \times 30 \times 30 \text{ mm}^3$) horizontally (length parallel to the start plate) using new powder, of which approximately 16 kg ended on the powder table, with the remaining 19 kg in the powder hoppers, following double fetch ARCAM Q10 plus settings. Following the virgin build, powder samples were collected from the top few layers at two regions in the powder bed: near-melt zone and away-melt zone as highlighted by red boxes in Figure 1. For the “recycled” condition, the powder bed of the same build volume as the virgin condition was preheated 10 times. The amount of powder available was lower than in the virgin builds since material was consumed in the sample blocks in the virgin build (~500 g) plus additional losses (~200 g) in each machine setup due to powder handling. After each preheat cycle the sintered ‘powder cake’ was treated in the ARCAM powder recovery system (PRS) and sieved (150 μm mesh sieve), while the unused powder left in the hopper were vacuumed and collected separately. Prior to powder reloading, sieved powder was manually mixed with unused powder from the hopper in each build, then poured back into the hopper. Following 10 preheat cycles, the second set of similar test coupons were fabricated. The unconsumed powder from the build was then recovered and sieved. Two powder samples were then collected after the PRS: sieve residues (powder that failed to pass through the sieve) and recycled powder (powder that passed through the sieve). Specimens for tensile, Charpy impact and fatigue tests were then extracted from the test coupons manufactured in both virgin and recycled condition. Mechanical test specimens were machined in accordance with ASTM E8-16, E23-16 and E466-15 standards.

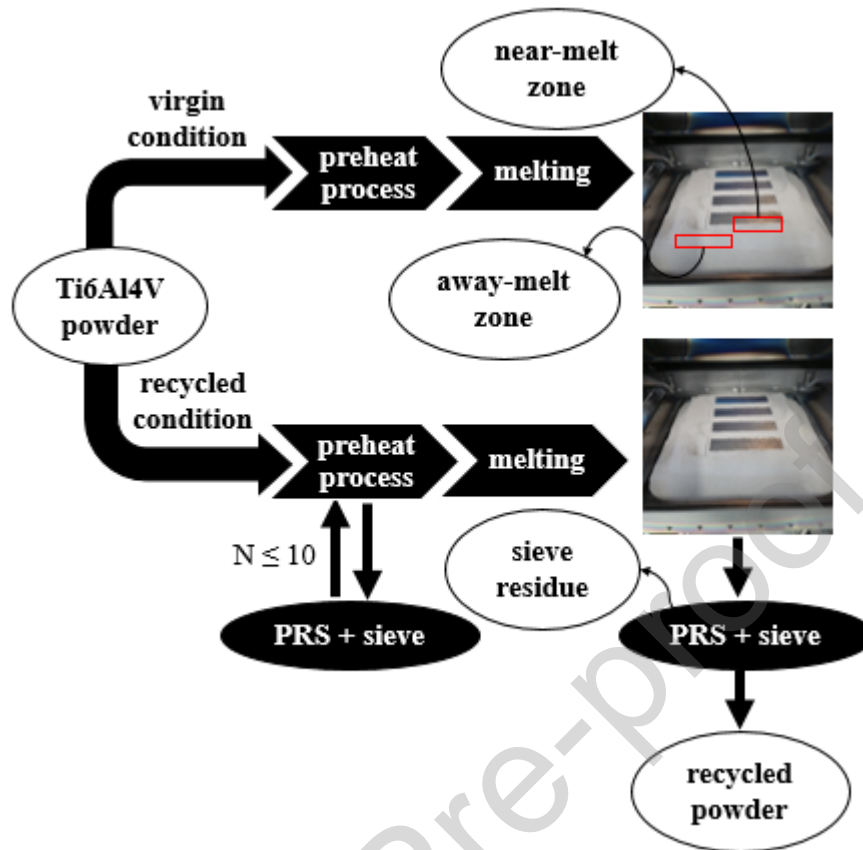


Figure 1. Powder sampling and manufacturing strategy used to fabricate test coupons following virgin and recycled conditions.

2.2 Manufacturing parameters

The applied EB-PBF process parameters for both conditions were based on the standard settings in auto calculation heat model software version 5.2.23 using 50 μm layer thickness. Prior to build, preparations included the adjustment of powder hopper baffles and fetching and rest positions after each run in order to guarantee the free flow of particles out of the hopper. This was because the powder showed different flow properties to standard ARCAM plasma-atomised powder. The preheat process was performed in two stages, preheat 1 and preheat 2, using a beam current of 22 and 26 mA respectively. Preheat 1 was applied over the entire build area (200 mm^2) and preheat 2 covered only the areas to be melted with 4 mm offset to build. Both preheats were performed using a defocused beam with a focus offset of 50 mA and scanning speed of 25000 mm/s to reduce the energy input enough to sinter the powder particles prior to melting. The initial preheating and post-heating aim to keep the temperature high enough to avoid powder smoke due to a decrease in powder bed temperature. Following preheats, which increased the build plate temperature to $\sim 750^\circ\text{C}$,

melting was applied using a focused beam, 36 mA focus offset, speed index of 60 at hatch spacing of 0.2 mm.

2.3 Powder characterisation

The O content was measured by inert gas fusion method while the Al and V contents were measured by inductively coupled plasma spectroscopy. Powder morphology was studied using a Zeiss EVO LS15 scanning electron microscope (SEM). Care was taken during powder mounting to avoid breaking sintered powder particles. SEM images were taken using the backscatter electron detector (BSE). In addition, quantitative powder shape analysis was performed using Morphologi 4-ID equipment. In both virgin and recycled powders, a large number of powder particles (>10000) were analysed using an automated-light microscope to provide statistical rigour. The 2D grayscale projections of the individual particles were filtered and classified using Morphologi 10.20 software. The projections were initially filtered using a particle transparency parameter; particles with a mean intensity level less than 100 pixels were not analysed. The images were then classified based on the particle shape parameters defined in [28] as spherical, satellites, fines and irregular categories based on the set-limits given in Table 1. Circularity is calculated by:

$$C_c = \sqrt{(4\pi A/P^2)} \quad (1)$$

where P and A refer to perimeter and projected area. Convexity is defined as:

$$C_x = P_c/P \quad (2)$$

where P_c refers to convex hull perimeter. Finally, elongation is defined as:

$$E = 1-AR \quad (3)$$

where AR refers to aspect ratio, *i.e.* the ratio of Feret's minimum to maximum length.

Table 1. Particle shape parameters used for classification of spherical, satellites, irregular, and fine Ti6Al4V EB-PBF powder particles for quantitative powder shape analysis.

Shape parameters	Circularity	Convexity	Elongation	Equivalent diameter / μm
Spherical	≥ 0.984	≥ 0.980	-	≥ 25
Satellites	0.874 to 0.985	< 0.997	< 0.294	≥ 25
Irregular	< 0.874	< 0.997	-	≥ 25
Fines	-	-	-	< 25

Laser diffraction was used to estimate powder particle size distribution (PSD) using a Malvern Panalytical Mastersizer 3000 system according to ASTM B822-17. A total of ten

iterations were performed for each powder sample. Liquid media (deionised water) was used as a carrier and no more than 25 g of powder was dispersed. The suspension was then circulated through the path of the laser light and 20 s circulation time elapsed before the measurement was taken. Powder flowability, apparent and tap densities were measured on virgin and recycled powders using PowderFlow kit supplied by LPW technologies UK, according to ASTM B213-17, B212-17 and B527-15 respectively. Ten measurements were made per powder sample to measure powder flowability using a hall flowmeter and three measurements were made per powder sample to measure the apparent and tap densities.

A Siemens D8 X-ray diffraction system with Cu K α source was used to identify the crystalline phases in the powder samples. Scans were performed with 2θ range between 20° and 80°. For metallographic examination of powders, care was taken during mounting and polishing to ensure homogeneity in material removal. The grinding was directly performed using 2500-grit SiC paper as using coarser grits can cause detachment of particles from the bakelite. Fine polishing was then performed down to 0.25 μm using diamond suspensions. Etching was made with Kroll's reagent (2 vol.% HF, 5 vol.% HNO₃, and 43 vol.% H₂O) by swabbing the polished surfaces for ~20 s to reveal the microstructure. SEM images were taken using backscattered electrons (BSE). Electron backscatter diffraction (EBSD) was performed on the powder samples using a Zeiss Sigma FEG-SEM at an accelerating voltage of 30 kV using AZtecHKL software. The data was post-processed using ATEX software [29]. A noise reduction factor of four was applied on all EBSD maps and high-angle grain boundaries (HAGB, $\theta > 15^\circ$) and low-angle grain boundaries (LAGB, $1.5^\circ < \theta < 15^\circ$) were plotted over the band contrast maps.

2.4 Build characterisation

The metallographic and mechanical test specimens were extracted from the same build height and in the same orientation (horizontal) from both the virgin and recycled test coupons to eliminate anisotropy effects that develop in EB-PBF builds [30]. The microstructure was studied along the build direction using secondary electron (SE) imaging mode in SEM. All of the mechanical tests were performed at room temperature.

Tensile testing was conducted on two specimens from both the virgin and recycled builds using a 100 kN capacity Instron servo-hydraulic test machine as per ASTM E8. Charpy impact testing was conducted on three specimens extracted from each of the virgin and recycled builds according to ASTM E23. Hardness testing was conducted using a

Vickers microhardness tester (Zwick/Roell ZHV μ) following ASTM E92 on as-polished samples. Six indents were made per sample at 1 kgf with a 10 s dwell time, and the average values with standard deviation are reported.

High cycle fatigue (HCF) testing was performed on four machined and polished (mirror surface finish, $<0.25 \mu\text{m}$) cylindrical specimens from both the virgin and recycled builds according to ASTM E466 using a 100 kN capacity Instron servo-hydraulic test machine. Cyclic loading was applied at a load ratio, $R = 0.1$; a maximum stress of 600 MPa, and at a frequency of 12 Hz. All specimens were tested until complete fracture. The fracture surfaces were examined under SEM. The surface area of the pores on the fracture surfaces was measured using ImageJ. The O, Al and V contents of the virgin and recycled test coupons were evaluated using the same methods as for the powders.

X-ray computed tomography (XCT) was performed on both virgin and recycled test specimens ($3 \times 3 \times 12 \text{ mm}^3$), using a laboratory-based XCT system (Nanofocus, Phoenix|X-ray). Each XCT scan was performed at 100 kV and 140 μA with a 0.34 mm thick copper filter, comprising 3142 radiographic projections with a 1 s exposure time per projection. These projections were reconstructed via filtered back project using the Datos|x software, resulting in an image matrix of $990 \times 990 \times 1000$ pixels with an isotropic voxel size of $13 \times 13 \times 13 \mu\text{m}^3$. The reconstructed image volume was subsequently analysed in Avizo 8.0 (Thermofisher Scientific) and Python. Firstly, the input image volume was deblurred by 3D unsharp masking (with a radius of 5 and an edge contrast of 0.5), for contrast enhancement and image sharpening. Secondly, the filtered image was then binarised by interactive thresholding. The volume fraction, porosity (%), and sphericity measurements were performed according to [31].

3. Results

3.1 Powder chemical composition

The O content of the powder and the test coupon increased by 0.02 wt.% (200 ppm) after 10 times of powder reuse, Table 2. It is interesting to note that the O content of the powder particles located near to the melt zone increased significantly by 0.04 wt.% (400 ppm) while the powder particles located away from the melt zone showed only marginal oxidation. The powder samples from the near- and away-melt zone regions were taken after the build was completed with the virgin powder. This indicates that the heterogeneity in powder oxidation could arise within a build. No significant change in the Al and V contents

was found between the virgin and recycled powder except for a marginal Al loss in the near-melt zone powder. In addition, the Al content in the test coupons was found to be lower compared with the powders. This is as expected because Al is a light element and its evaporation has been frequently reported during the EB-PBF process [25,32,33]. Nevertheless, the Al content was within the range specified in ASTM F3001.

Table 2: O, Al and V contents of EB-PBF Ti6Al4V powders in virgin, recycled, near-melt and away-melt zone conditions, and the builds.

Element (wt.%)	Virgin		Near-melt zone	Away- melt zone	Recycled		ASTM F3001
	Powder	Test coupon	Powder	Powder	Powder	Test coupon	
Oxygen	0.08	0.08	0.12	0.09	0.10	0.10	0.13 max.
Aluminium	6.57	5.86	6.10	6.48	6.44	5.87	5.50-6.50
Vanadium	4.18	4.13	4.10	4.22	4.16	4.14	3.50-4.50

3.2 Powder morphology and particle size distribution

Micrographs of the virgin and recycled powders are shown in Figure 2a-c and d-f respectively. At lower magnification (Figure 2a and d), both powders look similar. Most particles are spherical with some common features generally found in AGA powders such as satellites, elongations, irregularly shaped particles, agglomerates, and particles with open pores, as indicated by yellow arrows. However, a distinct difference in the powder surface morphology can be seen at high magnification. The virgin powder, Figure 2b and c, contains a significant number of fine particles (indicated by blue arrows) bonded to coarser particles. By comparison, the recycled powder shows craters (shallow depressions) and concave sites (deeper depressions) on the powder surface as indicated by red arrows in Figure 2e and f.

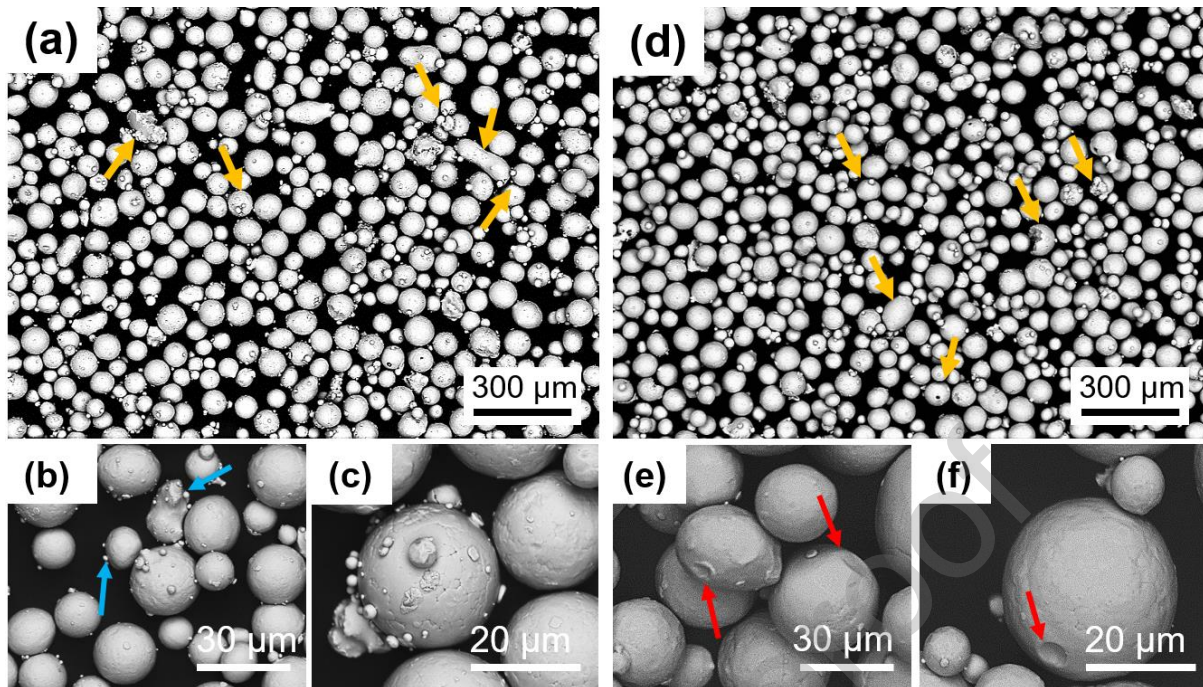


Figure 2. SEM image of EB-PBF Ti6Al4V (a-c) virgin and (d-f) recycled powders. Yellow arrows point the common features such as satellites, elongations, irregularly shaped particles, agglomerates, and particles with open porosities present in (a) and (d). Blue arrows point fine particles (b and c) in virgin powder. Red arrows point the craters (e) and concave sites (f) in recycled powder.

Morphologies of powder particles from near- and away-melt zone regions are shown in Figure 3. Particles close to the melt zone experience both preheats (preheat 1 and preheat 2) and are also exposed to the heat from the melt pool. Hence some of the particles from this region may partially melt (Figure 3a) or fuse with one another (hard-sintering, Figure 3b). However, the powder particles at the edges of the powder bed are exposed to relatively less heat, and thereby exhibiting soft-sintered morphology due to the preheating ($\sim 750^{\circ}\text{C}$) (Figure 3c).

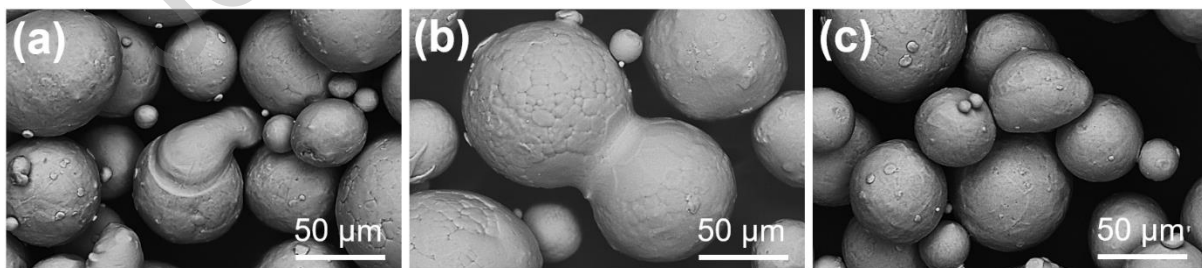


Figure 3. SEM BSE image of EB-PBF Ti6Al4V (a and b) near-melt zone and (c) away-melt zone powder morphology.

Figure 4a shows an illustration of the 2D particle radiographs, classified using the particle shape parameters listed in Table 1. The percentage of particles in each class is shown in Figure 4b. It can be seen that the recycled powder has 26% more spherical particles than

the virgin powder. In addition, the number of satellites and fine particles reduced by 10% and 30% respectively in the recycled powder. The near-melt zone powder contains a high fraction of satellites and irregular shaped particles due to sintering, and therefore has a low proportion of spherical particles.

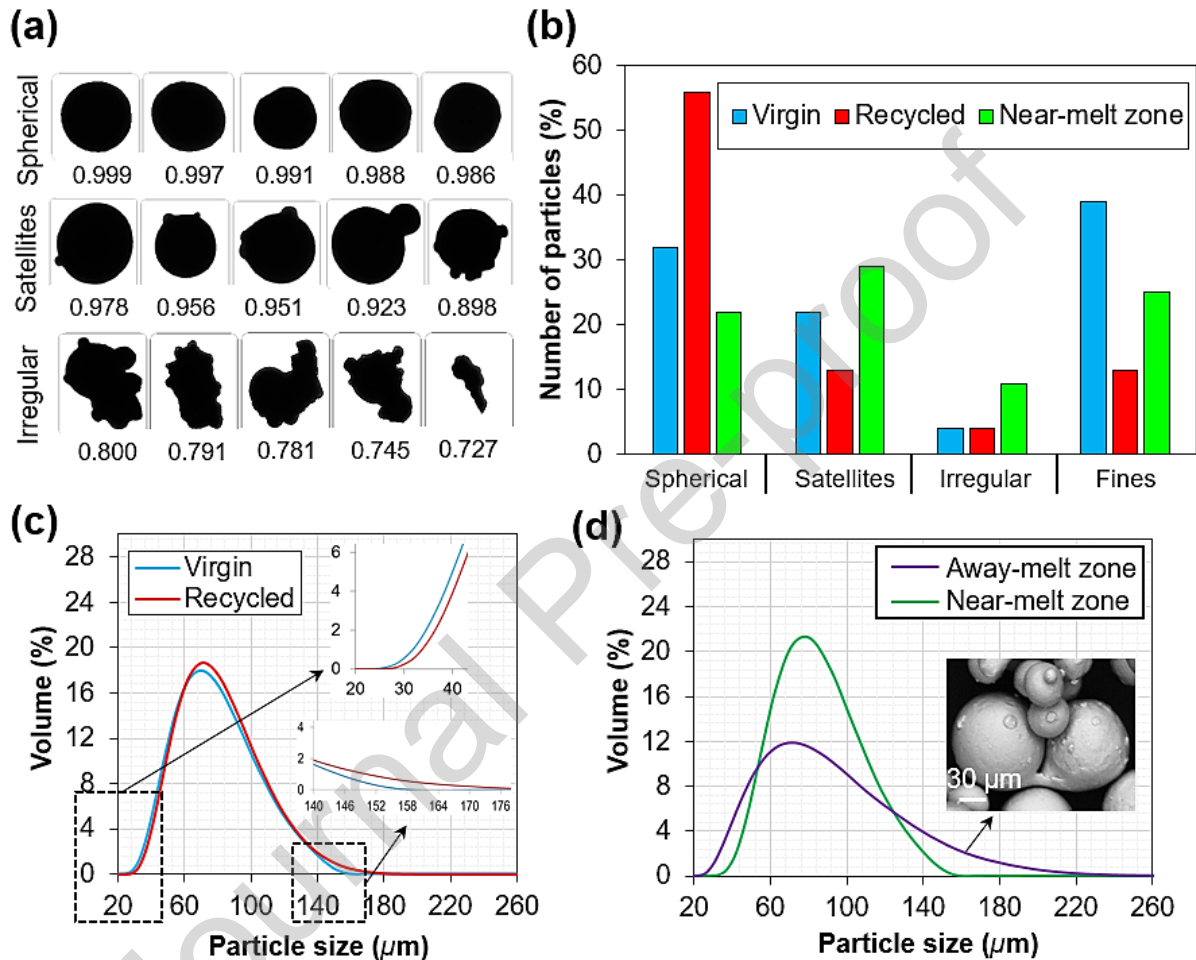


Figure 4. Quantitative powder shape and size analysis: (a) Illustration of classified 2D particle radiographs, the number below each radiograph corresponds to their circularity value (b) Shape analysis results of virgin, recycled, and near-melt zone powders; PSD of (c) virgin vs recycled and (d) away-melt zone vs near-melt zone powders measured by laser diffraction.

Figure 4c shows the PSD bell curves for the virgin and recycled powders. The respective $D_v(10)$, $D_v(50)$ and $D_v(90)$ values are 45, 69 and 105 μm for the virgin powder and 47, 71 and 107 μm for the recycled powder. It can be seen that the bell curve of the recycled powder has shifted slightly inwards at the finer side of the size spectrum and outwards at the coarser side (see the insets in Figure 4c). In terms of the PSD change with respect to locations in the powder bed, Figure 4d shows that the near-melt zone powder exhibits a wider PSD compared to the away-melt zone powder. The respective $D_v(10)$, $D_v(50)$ and $D_v(90)$

values are 45, 78 and 135 μm for the near-melt zone powder and 45, 69 and 105 μm for the away-melt zone powder.

Virgin and recycled powders exhibited a flowability of 26 ± 0.02 s/50g and 25 ± 0.02 s/50g respectively. Both powders exhibited continuous flow without any interruptions. In terms of apparent and tap densities, virgin powder exhibited 2.48 ± 0.01 gcm^{-3} and 3.03 ± 0.02 gcm^{-3} , while recycled powders showed 2.51 ± 0.01 gcm^{-3} and 3.09 ± 0.02 gcm^{-3} . The Hausner ratio (an empirical relationship that can be related to powder flowability [34]), was found to be 1.22 for the virgin and 1.23 for the recycled powders. Any values less than 1.25 are indicative of 'free-flowing' [35], hence both the virgin and recycled powders is judged to have a good flowability.

3.3 Powder microstructure

Micrographs of the virgin, away-melt zone, near-melt zone and recycled powder microstructures are shown in Figure 5. In the virgin condition (Figure 5a and b), the powder particles predominantly consisted of α' microstructure. However, the morphology of the α' laths depended on the particle size due to differences in the cooling rate during atomisation. The fine particle (Figure 5a), comprised long α' laths nucleated from particle edges and their growth continued until being interrupted by another α' lath from a different nucleation site (the inset of Figure 5a). This is due to the larger surface-to-volume ratio leading to higher cooling rate. By comparison, the coarser particle (Figure 5b) consisted majority of α' laths that were relatively short. This can be explained by the heterogeneous nucleation from several sites such as particle edges, material matrix and previously formed α' laths. The presence of a few longer laths (Figure 5b) could be attributed to the complex thermal cycles experienced during atomisation. Similar microstructural features were observed in the away-melt zone powder (Figure 5c).

In the case of near-melt zone powder, the hard-sintered powder particle, Figure 5d, had a heterogeneous microstructure with α' laths at one end (Figure 5d1) and coarser α laths with semi-continuous β phase boundaries (bright regions) at the other (Figure 5d2). By comparison, the loose powder particle from the same region comprised $\alpha+\beta$ microstructure (Figure 5e). The recycled powder contained particles with α' laths (Figure 5f) and particles with semi-continuous β phase between α laths (Figure 5g). XRD results in Figure 6 supports the SEM observations by revealing predominantly diffraction peaks of α/α' , hexagonal close-packed (HCP) phase. The near-melt zone and recycled powder showed a tiny peak (the insets

of Figure 6) that corresponds to β phase, body-centred cubic (BCC) structure, which was absent in the virgin and away-melt zone powders.

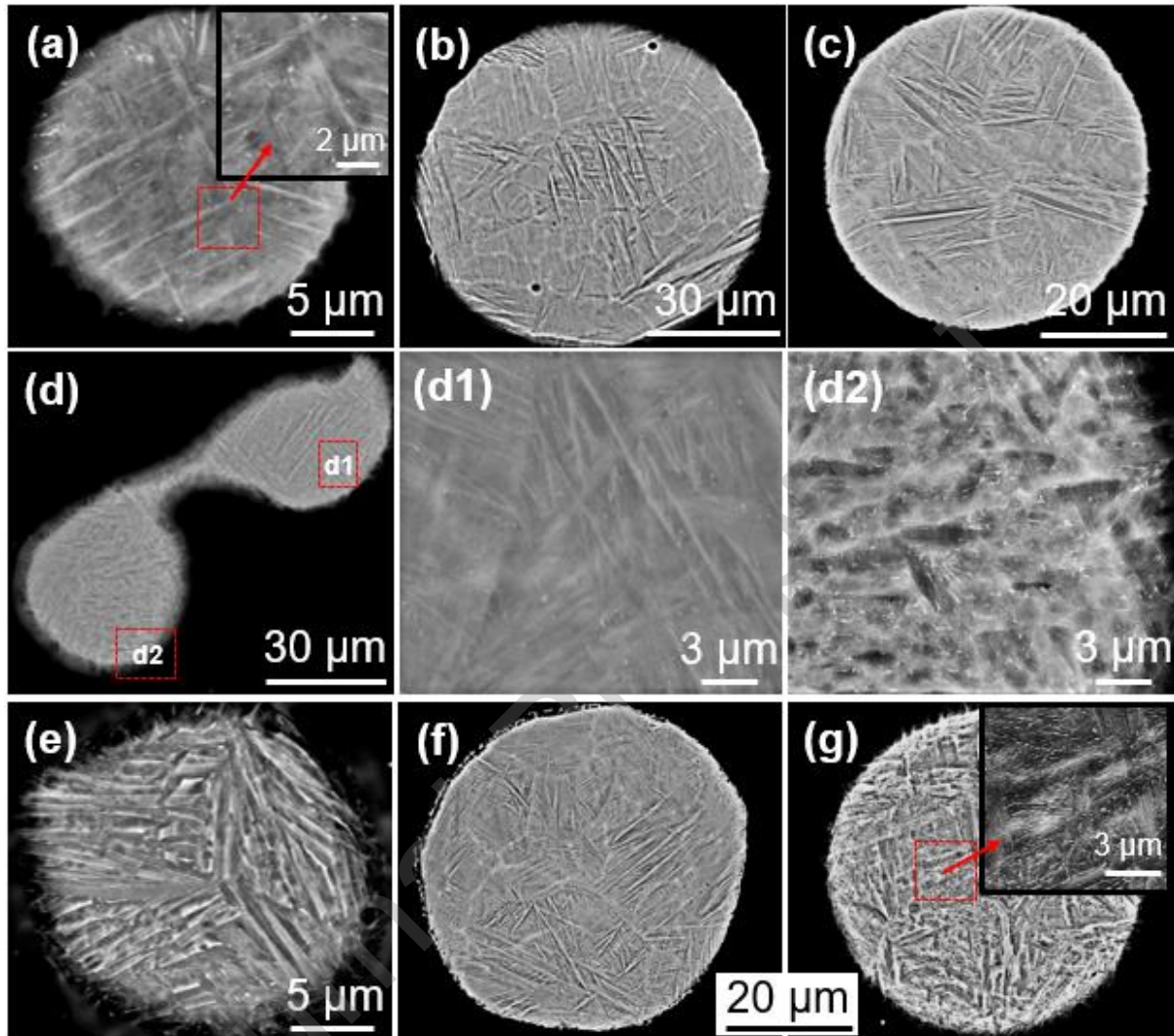


Figure 5. SEM BSE image of EB-PBF Ti6Al4V (a and b) virgin, (c) away-melt zone, (d-e) near-melt zone and (f and g) recycled powder microstructure.

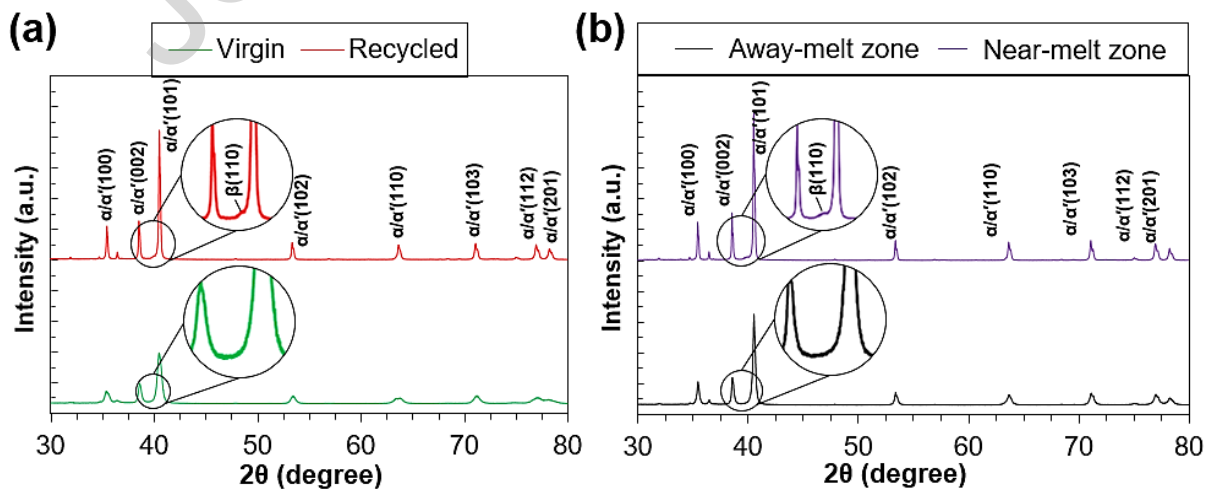


Figure 6. XRD pattern of EB-PBF Ti6Al4V (a) virgin vs recycled, (b) near-melt zone vs away-melt zone powders.

EBSD orientation maps were generated for virgin (Figure 7a) and near-melt zone (Figure 7b) powder particles based on the colour code in the inverse pole figure (IPF) (Figure 7c). The virgin powder particle consisted of randomly oriented α' laths that were roughly 3 to 34 μm in length. The α' laths mainly nucleated from the particle edges and other α' laths, supporting the SEM observations (Figure 5a and b). The near-melt zone powder particle, however, consisted of relatively thick α laths, with the majority of α laths oriented in the $\langle 100 \rangle$ crystallographic direction. The HAGB (red lines, $\theta > 15^\circ$) and LAGB (blue lines, $1.5^\circ < \theta < 15^\circ$) overlaid on the band contrast map of the virgin (Figure 7d) and recycled (Figure 7e) powder particle, show that the virgin powder particle had 19% LAGB and 81% HAGB while the near-melt zone powder particle contained 24% LAGB and 76% HAGB. This indicates a small reduction in high angle misorientation under the action of heating and slow cooling. The EBSD phase maps did not reveal any difference between the two powder particles (Supplementary Figure S1). This could be due to the relatively large step size of 0.3 μm employed, considering the thickness of β phase in EB-PBF Ti6Al4V that was reported to be ~ 50 nm [36].

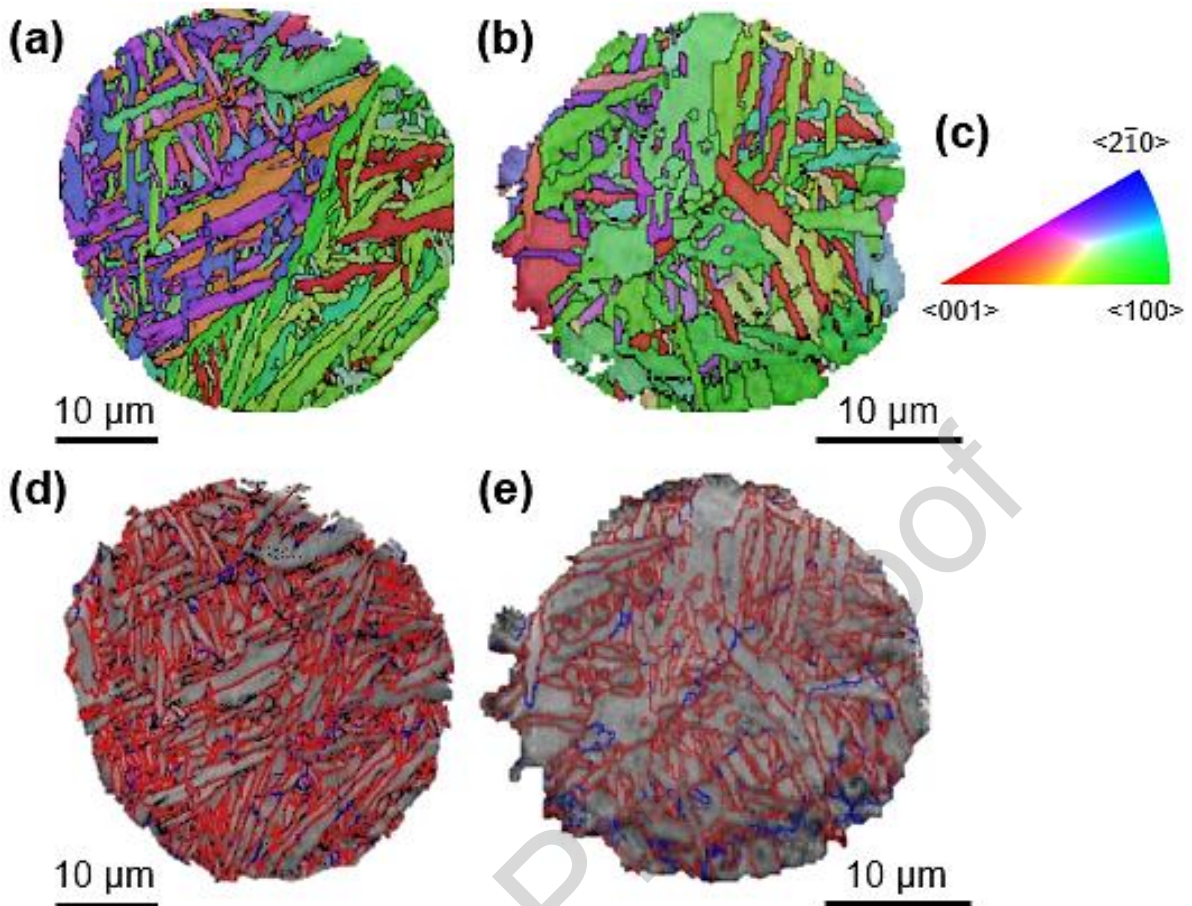


Figure 7. Orientation maps of virgin (a) and near-melt zone (b) powder particles based on the IPF (c). Band contrast map of the same virgin (d) and near-melt zone (e) powder particle with HAGB (red, $\theta > 15^\circ$) and LAGB (blue, $1.5^\circ < \theta < 15^\circ$).

3.4 Sieve residue

Sieving was used to remove the undesired coarse particles (larger than the mesh size of 150 μm) from entering into the subsequent builds and maintaining the PSD. Therefore, the sieve residue powder consisted of severely process affected particles such as: (1) hard-sintered particles (Figure 8a), formed by excessive heat exposure; (2) soft-sintered particles (Figure 8b, (red circle)) that were not broken in the PRS; and (3) agglomerates caused by melt ejections falling back into the powder bed (Figure 8c).

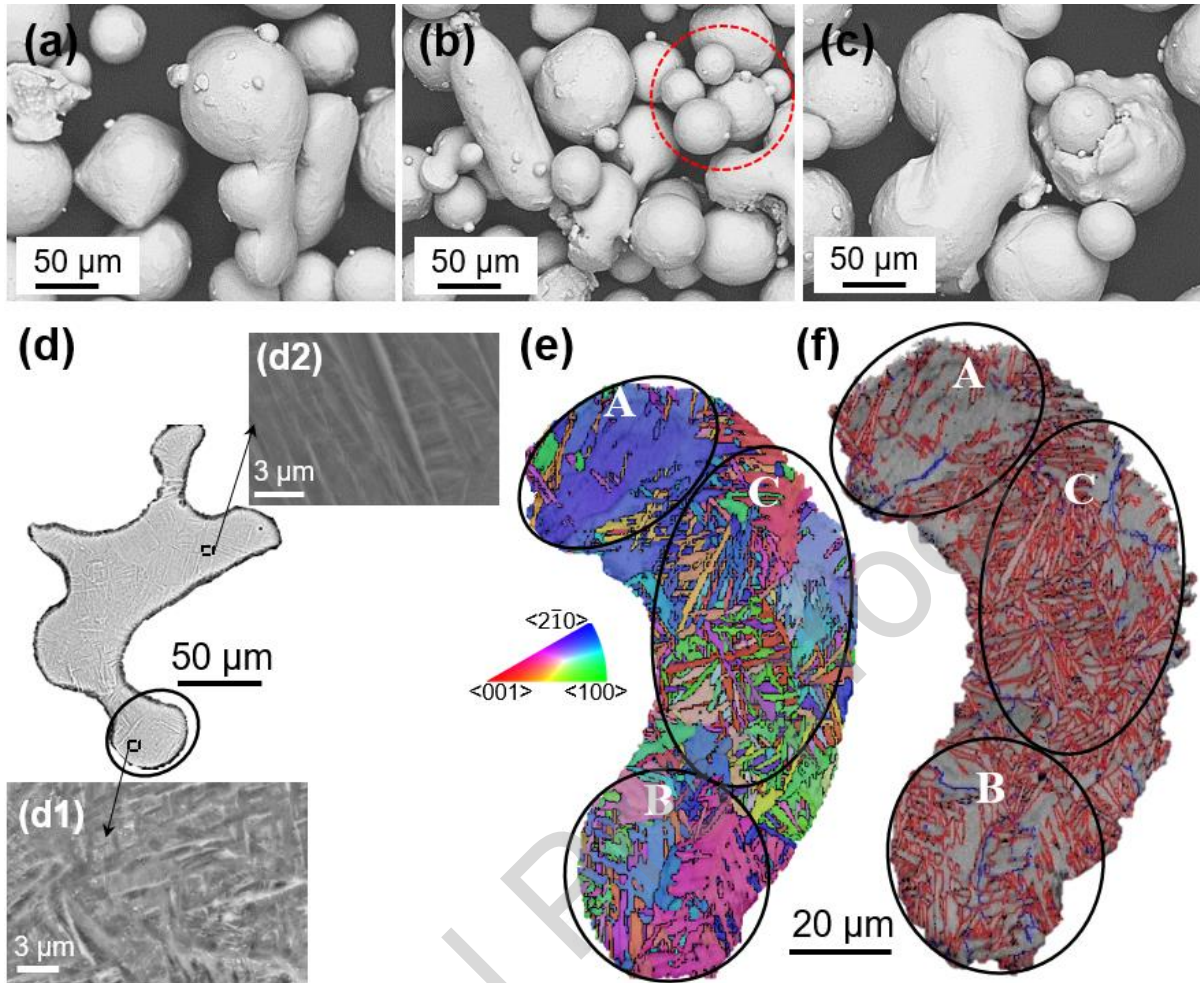


Figure 8. Ti6Al4V EB-PBF sieve residue: SEM image of powder particles, (a) hard-sintered, (b) unbroken soft-sintered (red circle) (c) agglomerated melt ejection. (d) The microstructure of a melt ejection that fell over a powder particle (indicated by the black circle); high magnification images of the (d1) powder particle and (d2) melt ejection regions; (e) orientation map with inset IPF and (f) band contrast map with HAGB (red) and LAGB (blue) of a melt ejection that fell over two powder particles.

Figure 8d shows the microstructure of a melt ejection that fell over a powder particle (indicated by black circle) in the powder bed and solidified. The high magnification image (Figure 8d1) of the powder particle region shows the presence of β phase between α laths while the melt ejection region has α' laths with no β phase (Figure 8d2). EBSD data of a melt ejection which fell over two powder particles is shown in Figure 8e and f. The selected particle for EBSD analysis appears to be similar to the particle shown in Figure 8c. It consists of three regions: two powder particle regions and one melt ejection region. The powder particle regions are designated as regions A and B while the melt ejection region corresponds to region C as indicated in the orientation (Figure 8e) and band contrast (Figure 8f) maps. Coarse α laths mainly oriented in the $\langle 2\bar{1}0 \rangle$ crystallographic direction was found in region A, while a few coarse α laths with orientations one halfway between $\langle 001 \rangle$ and $\langle 2\bar{1}0 \rangle$ and

other close to the $\langle 2\bar{1}0 \rangle$ direction was found in region B. Region C corresponded to the melt ejection region that had a mixture of acicular and coarse α laths with a size between 0.5-2.0 μm and 10-15 μm respectively. No preferred orientation was found for the acicular α laths, but the coarser α laths had two preferred orientations of close to $\langle 2\bar{1}0 \rangle$ and $\langle 001 \rangle$. The band contrast map with HAGB (red lines) and LAGB (blue lines) of each region in the particle is shown in Figure 8f. The melt ejection region with acicular α laths had a slightly higher fraction of HAGB than the powder particle regions with coarse α laths. Region A consisted of 24% LAGB and 76% HAGB, region B contained 22% LAGB and 78% HAGB and region C consisted of 85% HAGB and 15% LAGB.

3.5 Build properties

Microstructure in the build direction of the virgin and recycled test coupons extracted from the same location are shown in Figure 9a and b. A typical EB-PBF Ti6Al4V microstructure can be seen; grain boundary α (α_{GB}) and fine lamellar $\alpha + \beta$ phases (inset of Figure 9a1 and b1). The width of the lamellar α laths were measured as $0.49 \pm 0.11 \mu\text{m}$ for the virgin and $0.47 \pm 0.12 \mu\text{m}$ for the recycled test coupon.

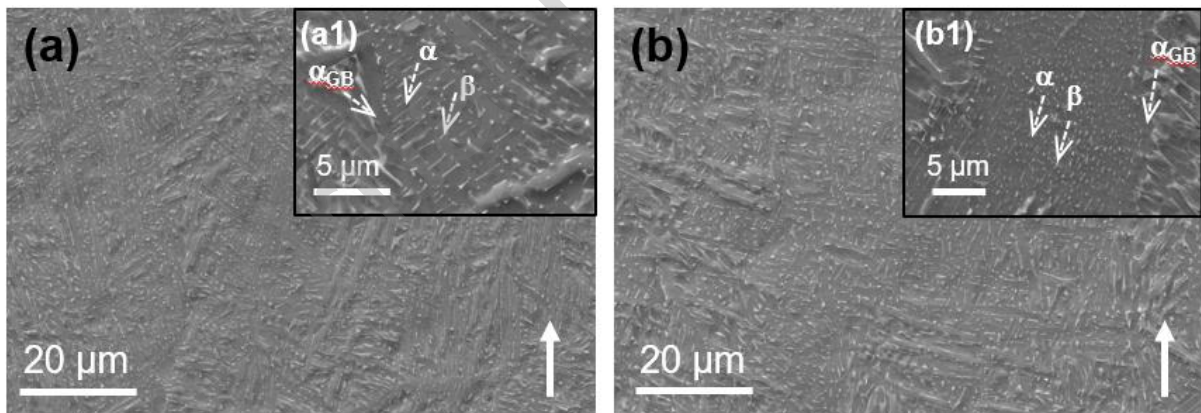


Figure 9. SEM SE image along build direction of EB-PBF Ti6Al4V specimens produced from (a) virgin and (b) recycled powder. Up-arrow indicates the build direction. The white-arrow in the insets indicate the presence of grain boundary α (α_{GB}) and lamellar α (dark regions) and β (bright regions).

Table 3 lists the tensile, Charpy impact, and Vickers hardness results of virgin and recycled EB-PBF test coupons together with as-cast Ti6Al4V material properties for comparison. The Vickers hardness values were the same for both the virgin and recycled builds. This is in good agreement with the microstructure observations, which showed the width of the α laths remained unchanged in the recycled test coupons. Similarly, the virgin and recycled builds had a similar value of Charpy impact energy. The tensile yield strength

(YS), ultimate tensile strength (UTS) and elongation (EL) of virgin and recycled test specimens were obtained from the stress-strain curves shown in Supplementary Figure S2. The tensile properties of both specimens are well above the minimum tensile property requirements mentioned in ASTM F3001 (Table 3). In addition, a marginal increase of 10 MPa in YS and UTS values of the recycled specimens was observed but the material elongation for both the specimens showed a negligible difference.

Table 3. Mechanical properties of virgin and recycled EB-PBF Ti6Al4V builds. ASTM F3001- minimum tensile properties of ELI Ti6Al4V produced by powder bed fusion AM

	YS _{0.2} / MPa	UTS / MPa	Elongation (EL) / %	Charpy impact energy/J	Vickers hardness / HV
Virgin	845 ± 0.5	918 ± 1	17 ± 1.05	47 ± 3.06	320 ± 7.57
Recycled	857 ± 1	928 ± 3.5	18 ± 0.68	45 ± 1.00	315 ± 5.20
ASTM F3001-14	795	860	10	-	-
As-cast [37]	738±11	853±24	12±1	-	-

HCF results of virgin and recycled specimens tested normal to the build direction are shown in Figure 10. Overall, the fatigue life decreased with powder reuse. The average fatigue life was $121,384 \pm 14,128$ cycles for the virgin builds and $99,759 \pm 8,287$ cycles for the recycled builds. An example of the fatigue fracture surface from the specimens produced using virgin and recycled powder that failed at 101,773 and 90,419 cycles are shown in Figure 10b and e, respectively. For both cases, fatigue cracks initiated at a surface defect/pore (Figure 10d and g). The crack initiated from a lack-of-fusion defect in the recycled specimen, whereas it initiated from a spherical gas pore in the virgin test specimen. In addition, embedded pores were found in both specimens as shown in Figure 10c and f, with their equivalent diameter being coarser in the recycled (86 μm) than in the virgin specimen (26 μm). Although the virgin specimen also contained larger embedded pores and larger lack-of-fusion defects like the recycled specimen (supplementary Figure S3), they were not located at the surface of the test specimens, hence being less detrimental to fatigue performance.

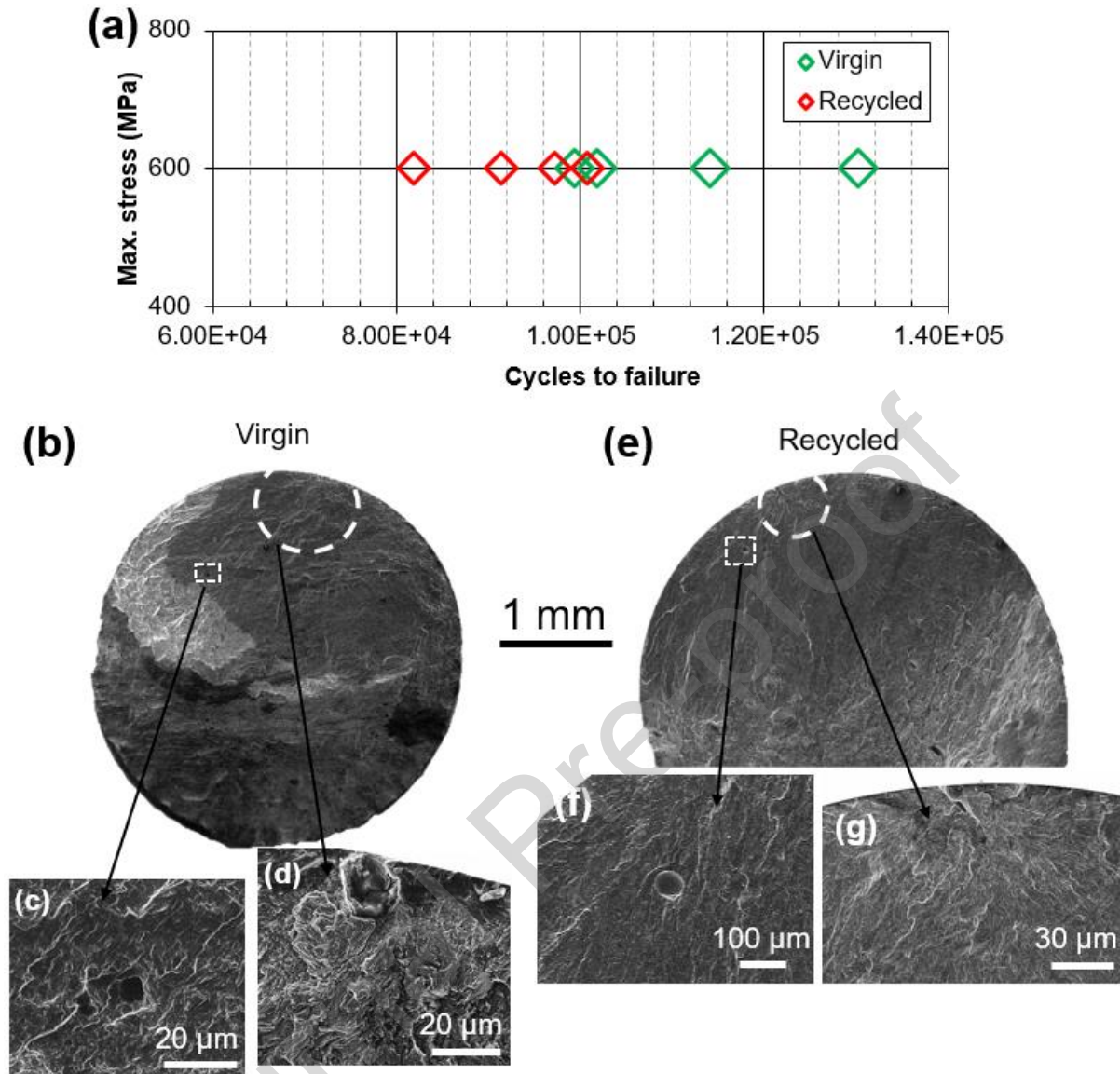


Figure 10. Fatigue life and SEM images of example fracture surfaces of EB-PBF Ti6Al4V specimens produced from virgin and recycled powder: (a) HCF results, (b) macrograph of virgin specimen, (c) crack initiation from a surface pore, (d) embedded small pores; (e) macrograph of recycled specimen, (f) crack initiation from a lack-of-fusion defect, (g) embedded large spherical pore.

In order to quantify the pore size distribution, X-ray CT scan was performed on virgin and recycled builds. Figure 11a and b show pores overlaid on volume rendered image of virgin and recycled specimens respectively with their corresponding equivalent diameters in the legend. The pores were randomly distributed in the samples, and their equivalent diameter ranged from 25 to 160 μm. The volume and number fraction of the pores in virgin and recycled builds are shown in Figure 11c and d. Both samples had a similar defect size distribution, Figure 11c. The porosity plot (Figure 11d) shows that the recycled builds had a marginal increase in small pores (with an equivalent diameter of < 50 μm). Meanwhile, there was a large increase (up to 50%) in large pores with an equivalent diameter from 50 to 160

μm compared to the virgin specimens. The average sphericity plot (Figure 11e) shows that the pores were less spherical in the recycled specimen, especially for the large pores with sizes from 80 to 160 μm . These irregular pores were likely to be the lack-of-fusion defects. The SEM fractography (Figure 10e) of the recycled specimen shows that fatigue cracks tended to initiate from lack-of-fusion defects with an equivalent diameter of 125 μm . Therefore, the recycled specimens have a higher number/volume of lack-of-fusion defects/pores than that of the virgin specimen.

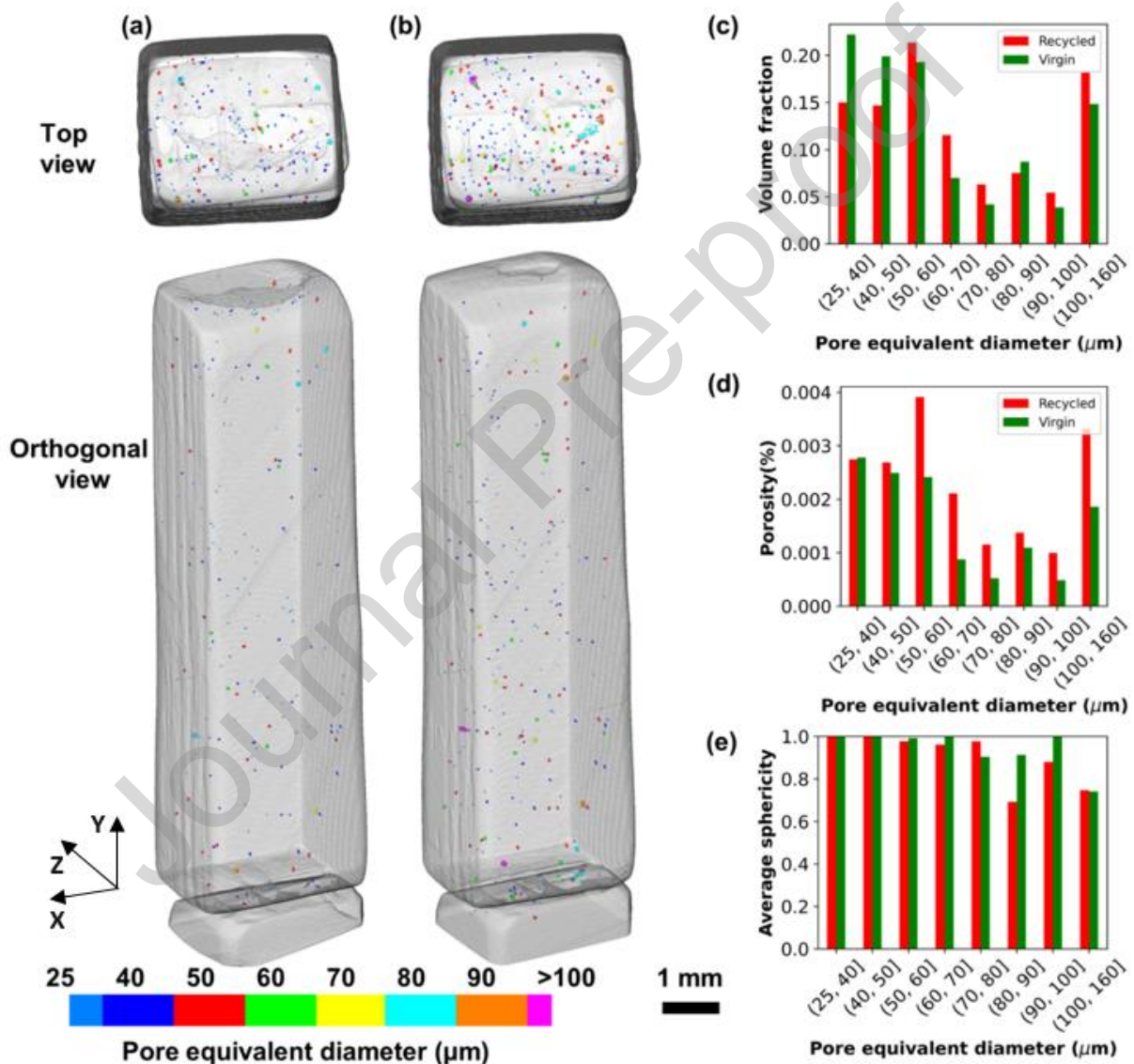


Figure 11. Pore quantification in virgin and recycled Ti6Al4V test specimen using X-ray computed tomography. 3D rendered images of pores overlaid on (a) virgin and (b) recycled test specimens. Z axis corresponds to the build direction. Defect (c) volume fraction, (d) porosity percentage and (e) sphericity as a function of pore equivalent diameter.

4. Discussion

A systematic approach was used to evaluate powder properties at various stages of recycling. Changes in powder characteristics during manufacturing and handling were assessed. Powder particles located at two different areas in the powder bed were investigated to estimate the changes in powder properties caused by melting and preheating. The powder recycled in a simulated manner for 10 build cycles was compared with the virgin powder to assess the effects of powder handling, recovery and reuse. The impact of powder recycling on part properties was also investigated by conducting microstructure characterisations and mechanical tests. The results have shown that the powder physical and chemical properties have changed after reusing for 10 times which altered the part properties such as tensile strength, fatigue and defect population. The link between powder and part property changes is discussed below.

4.1 Powder characteristics

Compared to the virgin powder, the used powder showed significant changes in the O content, morphology, PSD and microstructure. Ti6Al4V alloy has a high affinity with oxygen [24]. During powder recovery and re-loading, the powder particles tend to absorb moisture on its surface upon exposure to humidity in the atmosphere, which then breaks down into oxygen inside the EB-PBF machine chamber due to high temperature processing conditions. Since the alloy is highly oxidising at high temperatures (above 600°C), the dissociated oxygen can be picked up by the powder particles [18,38]. Therefore, an increase in the O content was observed in the recycled powder as shown in Table 2. Furthermore, due to the temperature gradient in the powder bed, the rate of powder oxidation varies at different areas in the powder bed. Powder particles at a higher temperature can oxidise more than particles at lower temperature in a given time [39]. Therefore, powder particles located closer to the melting area (near-melt zone), which gets exposed to both the preheat scans (preheat 1 and preheat 2) and latent heat from the melt pool exhibited a relatively higher O content than the away-melt zone particles. In addition, some fractions of light alloying elements like Al have also vaporised (Table 2) as the near-melt zone region was exposed to high temperature causing local powder particle melting (Figure 3). Nevertheless, the O and Al contents of all the powder samples stayed within the limit as specified in ASTM F3001.

Powder morphology and PSD play a vital role in determining the part density and surface roughness [12]. The virgin powder feedstock used in this study consisted of

significant number of fines, satellites and agglomerates, which are inherent features of the AGA powder [40] (Figure 2a-c, Figure 4b and c). After completion of each build cycle, the sintered powder bed was broken and recovered in the ARCAM PRS chamber using high velocity compressed air. This resulted in the formation of craters (shallow depressions) and concave sites (deeper depression) on the recycled powder surfaces (Figure 2e and f). We speculate that the craters could be attributed to the particle collisions and de-bonding of some strongly sintered particles as a result of multiple preheat scans. The concave sites could have been caused by the detachment of some satellite particles that had a weaker bond between the fine and coarse regions. Supporting evidence can be found from the quantitative shape analysis of the recycled powder (Figure 4b), which showed a significant reduction in the number of satellite particles. Therefore, the detached fine particles from satellites and other loose fine particles present in the virgin powder could have been blown-off by the compressed air flow to the powder collecting jug in PRS chamber. Hence a ~30% reduction in the number of fine particles and a marginal inward shift of the recycled powder PSD curve were observed (Figure 4b and c). The PSD curve shift appears to be marginal because the volume of a fine particle is low.

The formation of craters in the recycled powder would be unfavourable for a powder produced by plasma-based process, as they normally have higher sphericity in the as-manufactured condition [41]. However, in the case of AGA powder, the detachment of fine particles has increased powder sphericity (Figure 4b). In addition, the elimination of some fine particles with recycling has improved powder flowability by 4%, as fine particles have high surface energy and therefore are more cohesive [21,42]. Normally, a reduction in the number of fine particles tend to decrease the packing density of the powder bed, as the fine particles can fill the voids between the coarser particles [15]. On the contrary, there was only a marginal improvement in the packing density (2%). This could be due to the reduction in the number of satellite particles and improvement in powder sphericity which might have allowed the recycled powder to pack better.

The powder particles near the melt pool suffer maximum morphological degradation as shown in Figure 3a and b and Figure 4b and d. It is noteworthy that all the powder samples were sieved with 150 μm sieve before PSD measurement. However, some of the high aspect ratio particles (hard-sintered) managed to pass through the sieves, resulting in a coarser PSD and a marginal shift at the coarser side of the recycled powder PSD curve, see the insets of Figure 4d and c. The other severely sintered particles and agglomerates, were eliminated during sieving (Figure 8a and c). The minimal increase in the recycled powder flow,

considering the significant increase in powder sphericity and reduction in the fine particles could also be attributed to the presence of non-spherical high aspect ratio particles in the recycled powder. The away-melt zone powder which constitutes the majority of the recycled powder was only soft-sintered (Figure 3c). Therefore, it was easily broken in the PRS process and the unbroken soft-sintered particles were removed during sieving (Figure 8b, red circle). Hence, their PSD curve appears similar to that of the virgin powder. It is noteworthy that the number of fine and satellite particles in the near-melt zone region is higher than the recycled powder (Figure 4b, c and d). This is because the samples collected from these regions were directly sieved without being taken to the PRS chamber as the sample volume was less. This further confirms that the loose fine particles and the fine particles detached from the satellite particles are removed from the subsequent builds by the air flow in the PRS chamber during recycling, as also confirmed by Tang *et al.* [25].

The degree of microstructural change in a powder particle with reference to the initial powder provides a clear indication of the changes in powder properties that occurred during the EB-PBF manufacturing process. In addition, studying powder microstructure can be useful to interrogate the thermal histories and the corresponding O pick-up at different regions in the powder bed. The difference in powder O content has a major impact on the part properties [11,33,43]. To further investigate the microstructural changes, as the lamellar structures seen in Figure 5 are not clearly distinguishable, detailed investigation of the powder cross-section was performed by EBSD analysis (Figure 7).

The virgin powder particles consist of α' laths formed due to rapid cooling during the atomisation process. In the used powder, due to the high-temperature processing and temperature gradient in the powder bed, leading to complex thermal history in the powder particles during melting and repeated preheat scans, the particles at different regions of the powder bed are at different stages of $\alpha' \rightarrow \alpha + \beta$ transformation. Although most of the powder particles retained their initial martensitic microstructure, some of them consisted of non-continuous β phase on the lamellar boundaries of coarse α laths (Figure 5).

Any changes in the microstructure of the away-melt zone powder should be caused by preheat 1 scan, which was applied to the entire build area. During the EB-PBF process, the powders are held for a prolonged time at high temperatures, in this case, the build plate was maintained at a temperature of $\sim 750^\circ\text{C}$ for powder consolidation and residual stress development in the builds [44]. This elevated temperature can reduce the stacking faults formed in the powder during rapid solidification in the atomisation process [45], which is evident in the reduction of full-width half-maximum (FWHM) α/α' peaks, compared to the

virgin powder (Figure 6). Given that the preheat 1 scan involves the electron beam scanning the bed with a series of parallel lines, it is possible that some of the powder particles which were in the vicinity of the preheat 1 scan lines might have experienced high local temperatures, that were greater than the β -transus temperature and underwent certain level of $\alpha' \rightarrow \alpha + \beta$ transformation without reaching the melting point ($\sim 1650^\circ\text{C}$) [46]. On the other hand, it is likely that the temperature at the away-melt zone region would be lower by $\sim 70^\circ\text{C}$ of the set preheat temperature [47]. Nevertheless, since the analysed powder particles revealed no significant microstructural transformations (Figure 5) and showed no evidence of β peaks in the XRD plot, it is deduced that the powder particles at the edges of the powder bed were less affected by the EB-PBF processing conditions.

Due to the prolonged exposure of the near-melt zone powder particles to the heat from the melt pool and multiple preheat scans, significant changes were observed in their microstructure and crystal structure as illustrated in Figure 6, Figure 5d-e, and Figure 7b and e. Holding the material at high temperatures close to β -transus followed by slow cooling can lead to $\alpha' \rightarrow \alpha + \beta$ transformation, due to dissociation of β -stabilizing elements such as vanadium rich elements from α phase to their lamellar boundaries, forming β phase [48]. This dissociation is generally followed by the coarsening of α laths in Ti6Al4V powders [24], which explains the formation of coarse α laths in Figure 5d2, e and g; corresponding to the β peak observed in Figure 6. In addition, the slow conductional heat loss due to high-temperature powder bed ($\sim 750^\circ\text{C}$), has resulted in the reduction of randomness in α lath orientation and local crystallographic misorientations. However, the transformed microstructure could be inhomogeneous like that shown in Figure 5d, where one region had β phase between the α laths while the other had only α' microstructure. This could be attributed either to partial exposure of the particle to the heat, or heat dissipation from the particle to the surrounding.

The recycled powder (Figure 5f and g) includes powder particles from both the near-melt zone and away-melt zone regions. Therefore, the recycled powder microstructure consists of particles with both α' and particles with coarse α laths that are at different stages of $\alpha' \rightarrow \alpha + \beta$ phase transformation and the small β peak found in the recycled powder could be attributed to the presence of few fractions of near-melt zone particles in the recycled powder (Figure 6).

Montelione et al [49] have shown that the powder particles with a coarser microstructure had thicker oxide layers, supporting that the near-melt zone powder that consists of coarser microstructure (Figure 5 and Figure 7), had higher O content (Table 2).

However, no intermetallic (Ti_3Al) precipitates were found in any of the powder particles investigated. This is as expected because the O content needs to exceed ~ 0.35 wt.% to trigger such phase transformation [50]. Hence, it is likely that no excessive local powder oxidation occurred due to high local temperatures caused by the temperature gradient during preheating and melting.

Investigation of the sieve residue provides a better understanding of powder degradation, as it contains the severely process affected particles that provides a great potential for correlation between powder property changes to EB-PBF recycling methods. For example, hard sintered particles found in the near-melt zone due to high temperatures, unbroken soft-sintered particles found in the away-melt zone region and melt ejections (Figure 8). Unlike laser additive manufacturing, melt ejections are seldom observed in electron beam additive manufacturing. Melt ejection in EB-PBF process can occur owing to the turbulence formed in the melt pool due to the interaction of various forces such as vapour pressure, beam to powder bed/substrate inconsistencies and charge interactions [51]. On the other hand, appearance of melt ejections indicates that the standard ARCAM process settings might need to be tuned while using AGA powders.

Morphology and microstructure analysis of the melt ejections present in the sieve residue was performed (Figure 8). The melt ejection that exited the melt pool during fabrication, fell back into the powder bed and formed powder agglomerations (Figure 8c). As most of these agglomerates were relatively coarse (a few mm in size), they were removed by sieving. However, it is possible that ejection of certain volume of melt pool in the form of spatter, could lead to increased defects in the build parts. Anwar *et al.* [52] have reported that the distribution of ejections is higher at the near-melt zone region of the powder bed in the L-PBF process. Since EB-PBF process is performed in vacuum and there is no gas flow through the chamber during manufacturing as in the L-PBF, it is speculated that these melt ejections were present in the near-melt zone region of the powder bed.

Microstructure and EBSD analysis performed on a melt ejection that fell over two powder particles revealed heterogeneity in phases and α lath morphologies. The powder particle regions, had coarse α laths with reduced local misorientations (Figure 8d1, e, f). This might be due to the annealing effect associated with the heat transfer either from the deposited melt ejection to the powder particle regions or from the melt pool over that particular region. The melt ejection region (region C) had a high fraction of α' laths and high local misorientations, which could be due to rapid cooling during of the melt ejection during the flight before falling into the powder bed. However, some parts of the melt ejection region

had coarser α laths that could have been caused by high temperature in the powder bed that resulted in slow cooling or the heat from the melt pool on that region of the melt ejection.

Therefore, the present study shows that Ti6Al4V powder microstructural changes do occur and are subject to the location of the powder particles in the powder bed. However, it should be noted that the quantity of heat-affected powder particles that possess deformed powder morphology, transformed microstructure and high O level increases with the number of recycling iterations and when large build volume is utilised for processing. As the current study analysed only one particle in each condition, further statistical analysis is required to correlate the change in powder microstructure to chemical composition.

4.2 Build properties

Test specimens were extracted from the same location and orientation (horizontal) in both the virgin and recycled test coupons to eliminate the effect of anisotropy. Results revealed negligible impact of powder preheating, recovery and reuse on microstructure, Charpy impact energy and hardness values. As shown in Table 2, the recycled test specimen has higher O content than the virgin specimen. Normally, an increase in O content has a negative impact on the damage tolerance of EB-PBF Ti6Al4V. However, in the present study, the O content in both specimens did not exceed the maximum limit (0.13 wt.%). Therefore, no obvious difference was found in the microstructure (Figure 9) and thereby the hardness values. Similarly, no reduction in Charpy impact values was observed in the recycled specimen.

The effects of EB-PBF powder recycling on tensile properties of Ti6Al4V have been widely reported in several studies [23,25,53]. Most commonly reported phenomena were the increase in YS and UTS of the specimen with recycling. In the present work, the YS and UTS showed a marginal increase with recycling (Table 3). The main cause for this behaviour is the increase in O content from 0.08 wt.% (800 ppm) to 0.1 wt.% (1000 ppm) after recycling. Oxygen in Ti6Al4V acts as α -stabiliser [50] and provides strength by creating a solid-solution in the α phase [43,54]. It occupies octahedral sites creating lattice strain in the c direction of the HCP structure and thereby affecting the interactions between dislocations [55]. Therefore, along with increasing strength, a decrease in material elongation at high O content has also been reported in some studies [23,56]. However, in the present work, the increase in O level was marginal (0.02 wt.%) and was well below the maximum O limit (0.13 wt.%) in contrast to the previous work, where the material O content exceeded 0.2 wt.%.

(Ti6Al4V Gr.5 O wt.% max.) Therefore, negligible impact was observed on the material elongation.

HCF testing was conducted in the machined and polished condition at a single stress level on the virgin and recycled test specimens (Figure 10a). The scatter in the obtained data in both cases is due to the presence of defects/pores with a wide range of sizes in both types of specimens (Figure 11). The average fatigue life of the recycled specimen is lower than the virgin. All the specimens in both the virgin and recycled conditions failed from surface pores/defects. In terms of pores/defect sizes, the fracture surface and XCT scan results show pore sizes of 25 to 160 μm in both the virgin and recycled test specimens. This observation aligns with the previous work [21,57] where the increased number of large-sized pores were found with the powder reuse in L-PBF process. Furthermore, with respect to defect morphology, a relatively larger fraction of lack-of-fusion defects were present in the recycled specimens (Figure 11c-e). Lack-of-fusion defects are more detrimental than spherical gas porosities [58]. Therefore, two out of four recycled specimens, which had the lowest fatigue life, failed from the lack-of-fusion defect (Figure 10e), reducing the average fatigue life of the recycled specimen.

The increase in the number and volume fraction of lack-of-fusion defects in the recycled specimen could be attributed to powder morphological degradation. Therefore, although repetitive PRS treatment can improve powder sphericity and could provide better spreadability of a used powder during the build process, the presence of some heat-affected particles with high aspect ratio, coupled with reduction in the number of fine particles, can create more voids in a powder layer. This very likely promoted the higher fraction of lack-of-fusion defects as observed in the recycled test specimens.

The current study provides fundamental insights into the different types of changes in individual powder particle properties, the related mechanisms which influence bulk powder behaviour and affect the build quality. However, there are some limitations worthwhile for commenting. The current study employed a simulated method to recycle powder involving preheats alone. Although it was effective in demonstrating the effect of preheat cycles on powder properties, some of the effects of repetitive melting and post-heating were not accounted for. Therefore, it is expected that in the actual powder recycling process, the magnitude of changes in powder and build properties may be higher, depending on the number of reuse times, build volume, process parameters etc.

5. Conclusions

The changes in powder physical and chemical properties during manufacturing and handling in electron-beam powder bed fusion (EB-PBF) process and its subsequent impact on Ti6Al4V build properties were investigated. The following conclusions can be drawn:

- (i) Powder particles at the near-melt zone region suffer maximum degradation. Results revealed powder morphological degradation such as hard-sintering, partial melting and agglomerations. The hard-sintered high aspect ratio particles managed to pass through the sieves affecting the recycled powder quality. Other powder physical property changes included larger particle size distribution, α lath coarsening, β precipitation and reduction of randomness in crystal orientations. The near-melt zone powder particles had higher oxidation rate than the particles in the away-melt zone region.
- (ii) Powder particles at the away-melt zone region are soft-sintered due to powder bed preheating. A slight increase in O content with no change in microstructure was observed. The soft-sintered particles can be broken down and recycled.
- (iii) Virgin vs recycled powder: The recycled powder had better sphericity, improved flow and packing behaviour. The virgin powder had α' microstructure while recycled powder had particles with α' and particles being subjected to different stages of $\alpha' \rightarrow \alpha + \beta$ microstructural transformation. O content in the recycled was found to be 25% higher than virgin powder.
- (iv) Virgin vs recycled build: There was no significant difference in the microstructure, Charpy impact energy, hardness, and elongation values. There was a marginal increase in YS and UTS (10 MPa) due to the slight increase in recycled powder O content. The reduction in the fatigue life of the recycled builds was due to the increase in lack-of-fusion defects in recycled builds. It is possible that the voids formed in the powder bed could be due to the coupled effect of reduced number of fines and presence of high aspect ratio powder particles in the used powder that led to the formation of lack-of-fusion defects.

Author Contributions

Gowtham Soundarapandiyam: Conceptualization, Methodology, Investigation, Writing - Original Draft, Visualization. **Carol Johnston:** Supervision, Writing - review & editing, Resources, Project administration. **Raja H.U. Khan:** Supervision, Conceptualization, Investigation, Resources, Writing - review & editing, **Chu Lun Alex Leung:** XCT

experiment and analysis, Writing - Review & Editing, **Peter D. Lee:** Resources, **Everth Hernandez-Nava:** Methodology- Specimen preparation, Resources, Writing- review & editing. **Bo Chen:** Supervision, Investigation, Data Curation, Writing - review & editing. **Michael E. Fitzpatrick:** Supervision, Conceptualization, Resources, Writing - review & editing, Funding acquisition.

Acknowledgements

This research was made possible by the sponsorship and support of the Lloyd's Register Foundation, a charitable organisation that helps to protect life and property by supporting engineering-related education, public engagement and the application of research. The authors would like to thank LPW Technology and University of Sheffield for providing powder feedstock and fabricating specimens respectively. The work was enabled through and conducted at the National Structural Integrity Research Centre (NSIRC) managed by TWI through a network of both national and international Universities. The financial support from the EPSRC Fellowship EP/R043973/1 awarded to Bo Chen is acknowledged to facilitate this research collaboration. The authors acknowledge the XCT facility and analysis at the Research Complex at Harwell (RCaH), funded through the UK-EPSRC MAPP: Future Manufacturing Hub in Manufacture using Advanced Powder Processes ([EP/P006566/1](#)) and a Royal Academy of Engineering Chair in Emerging Technology (CiET1819/10). EH-N would like to acknowledge the Henry Royce Institute for Advanced Materials, funded through EPSRC grants EP/R00661X/1, EP/S019367/1, EP/P02470X/1 and EP/P025285/1 for access to the ARCAM Q10+ system at The University of Sheffield. C.L.A.L. is grateful for the EPSRC grant (EP/R511638/1) to work on this project

References

- [1] L.E. Murr, Metallurgy of additive manufacturing: Examples from electron beam melting, *Addit. Manuf.* 5 (2015) 40–53. <https://doi.org/10.1016/j.addma.2014.12.002>.
- [2] W. Gao, Y. Zhang, D. Ramanujan, K. Ramani, Y. Chen, C.B. Williams, C.C.L. Wang, Y.C. Shin, S. Zhang, P.D. Zavattieri, The status, challenges, and future of additive manufacturing in engineering, *CAD Comput. Aided Des.* 69 (2015) 65–89. <https://doi.org/10.1016/j.cad.2015.04.001>.
- [3] K. V. Wong, A. Hernandez, A Review of Additive Manufacturing, *ISRN Mech. Eng.*

- 2012 (2012) 1–10. <https://doi.org/10.5402/2012/208760>.
- [4] D.A. Ramirez, L.E. Murr, E. Martinez, D.H. Hernandez, J.L. Martinez, B.I. MacHado, F. Medina, P. Frigola, R.B. Wicker, Novel precipitate-microstructural architecture developed in the fabrication of solid copper components by additive manufacturing using electron beam melting, *Acta Mater.* 59 (2011) 4088–4099. <https://doi.org/10.1016/j.actamat.2011.03.033>.
- [5] S. Price, J. Lydon, K. Cooper, K. Chou, Experimental temperature analysis of powder-based electron beam additive manufacturing, 24th Int. SFF Symp. - An Addit. Manuf. Conf. (2013) 162–173.
- [6] Z.C. Cordero, H.M. Meyer, P. Nandwana, R.R. Dehoff, Powder bed charging during electron-beam additive manufacturing, *Acta Mater.* 124 (2017) 437–445. <https://doi.org/10.1016/j.actamat.2016.11.012>.
- [7] E. Hernández-Nava, S. Tammam-Williams, C. Smith, F. Leonard, P.J. Withers, I. Todd, R. Goodall, X-ray Tomography Characterisation of Lattice Structures Processed by Selective Electron Beam Melting, *Metals (Basel)*. 7 (2017). <https://doi.org/10.3390/met7080300>.
- [8] J. Raplee, A. Plotkowski, M.M. Kirka, R. Dinwiddie, A. Okello, R.R. Dehoff, S.S. Babu, Thermographic Microstructure Monitoring in Electron Beam Additive Manufacturing, *Sci. Rep.* 7 (2017) 1–16. <https://doi.org/10.1038/srep43554>.
- [9] A.T. Sutton, C.S. Kriewall, M.C. Leu, J.W. Newkirk, Powders for additive manufacturing processes: Characterization techniques and effects on part properties, in: *Solid Free. Fabr. Proc.*, 2016: pp. 1004–1030. <https://doi.org/10.1080/17452759.2016.1250605>.
- [10] A. Strondl, O. Lyckfeldt, H. Brodin, U. Ackelid, Characterization and Control of Powder Properties for Additive Manufacturing, *Jom.* 67 (2015) 549–554. <https://doi.org/10.1007/s11837-015-1304-0>.
- [11] C.L.A. Leung, S. Marussi, M. Towrie, R.C. Atwood, P.J. Withers, P.D. Lee, The effect of powder oxidation on defect formation in laser additive manufacturing, *Acta Mater.* 166 (2019) 294–305. <https://doi.org/10.1016/j.actamat.2018.12.027>.
- [12] M.J. Heiden, L.A. Deibler, J.M. Rodelas, J.R. Koepke, D.J. Tung, D.J. Saiz, B.H.

- Jared, Evolution of 316L stainless steel feedstock due to laser powder bed fusion process, *Addit. Manuf.* 25 (2019) 84–103. <https://doi.org/10.1016/j.addma.2018.10.019>.
- [13] E. Santecchia, P. Mengucci, A. Gatto, E. Bassoli, S. Defanti, G. Barucca, Cross-Contamination Quantification in Powders for Additive Manufacturing: A Study on Ti-6Al-4V and Maraging steel, *Materials (Basel)*. 12 (2019). <https://doi.org/10.3390/ma12152342>.
- [14] AMS7000, Laser-Powder Bed Fusion (L-PBF) Produced Parts, Nickel Alloy, Corrosion and Heat-Resistant, 62Ni - 21.5Cr - 9.0Mo - 3.65Nb Stress Relieved, Hot Isostatic Pressed and Solution Annealed, *SAE Int. J. Aerosp.* (2018).
- [15] L.C. Ardila, F. Garciandia, J.B. González-Díaz, P. Álvarez, A. Echeverria, M.M. Petite, R. Deffley, J. Ochoa, Effect of IN718 recycled powder reuse on properties of parts manufactured by means of Selective Laser Melting, *Phys. Procedia*. 56 (2014) 99–107. <https://doi.org/10.1016/j.phpro.2014.08.152>.
- [16] B.A. Hann, Powder Reuse and Its Effects on Laser Based Powder Fusion Additive Manufactured Alloy 718, (2016). <https://doi.org/10.4271/2016-01-2071>.
- [17] L. Cordova, M. Campos, T. Tinga, Revealing the Effects of Powder Reuse for Selective Laser Melting by Powder Characterization, *Jom*. 71 (2019) 1062–1072. <https://doi.org/10.1007/s11837-018-3305-2>.
- [18] P. Nandwana, W.H. Peter, R.R. Dehoff, L.E. Lowe, M.M. Kirka, F. Medina, S.S. Babu, Recyclability Study on Inconel 718 and Ti-6Al-4V Powders for Use in Electron Beam Melting, *Metall. Mater. Trans. B*. 47 (2016) 754–762. <https://doi.org/10.1007/s11663-015-0477-9>.
- [19] H. Gruber, M. Henriksson, E. Hryha, L. Nyborg, Effect of Powder Recycling in Electron Beam Melting on the Surface Chemistry of Alloy 718 Powder, *Metall. Mater. Trans. A*. 50 (2019) 4410–4422. <https://doi.org/10.1007/s11661-019-05333-7>.
- [20] A.H. Maamoun, M. Elbestawi, G.K. Dosbaeva, S.C. Veldhuis, Thermal post-processing of AlSi10Mg parts produced by Selective Laser Melting using recycled powder, *Addit. Manuf.* 21 (2018) 234–247. <https://doi.org/10.1016/j.addma.2018.03.014>.

- [21] V. Seyda, N. Kaufmann, C. Emmelmann, Investigation of Aging Processes of Ti-6Al-4 v Powder Material in Laser Melting, *Phys. Procedia*. 39 (2012) 425–431. <https://doi.org/10.1016/j.phpro.2012.10.057>.
- [22] P.E. Carrion, A. Soltani-Tehrani, N. Phan, N. Shamsaei, Powder Recycling Effects on the Tensile and Fatigue Behavior of Additively Manufactured Ti-6Al-4V Parts, *Jom*. 71 (2019) 963–973. <https://doi.org/10.1007/s11837-018-3248-7>.
- [23] M.B. Vladimir Popov, Alexander Katz-Demyanetz, Andrey Garkun, The effect of powder recycling on the mechanical properties and microstructure of electron beam melted Ti6Al4V specimens, *Addit. Manuf.* 22 (2018) 834–843. <https://doi.org/10.1016/j.addma.2018.06.003>.
- [24] Y. Sun, M. Aindow, R.J. Hebert, The effect of recycling on the oxygen distribution in Ti-6Al-4V powder for additive manufacturing, *Mater. High Temp.* 35 (2017) 217–224. <https://doi.org/10.1080/09603409.2017.1389133>.
- [25] H.P. Tang, M. Qian, N. Liu, X.Z. Zhang, G.Y. Yang, J. Wang, Effect of Powder Reuse Times on Additive Manufacturing of Ti-6Al-4V by Selective Electron Beam Melting, *Jom*. 67 (2015) 555–563. <https://doi.org/10.1007/s11837-015-1300-4>.
- [26] V. Petrovic, R. Niñerola, Powder recyclability in electron beam melting for aeronautical use, *Aircr. Eng. Aerosp. Technol.* 87 (2015) 147–155. <https://doi.org/10.1108/AEAT-11-2013-0212>.
- [27] F.J. Alamos, J. Schiltz, K. Kozlovsky, R. Attardo, C. Tomonto, T. Pelletiers, S.R. Schmid, Effect of powder reuse on mechanical properties of Ti-6Al-4V produced through selective laser melting, *Int. J. Refract. Met. Hard Mater.* 91 (2020) 105273. <https://doi.org/10.1016/j.ijrmhm.2020.105273>.
- [28] E. Olson, Particle shape factors and their use in image analysis-part 1: theory, *J. GxP Compliance*. 15 (2011) 85–96.
- [29] J.-J.F. B. Beausir, Analysis Tools for Electron and X-ray diffraction, ATEX - Software, [Www.Atex-Software.Eu](http://www.atex-software.eu), Univ. Lorraine. (2017). <http://www.atex-software.eu/>.
- [30] H. Sharma, D. Parfitt, A.K. Syed, D. Wimpenny, E. Muzangaza, G. Baxter, B. Chen, A critical evaluation of the microstructural gradient along the build direction in

- electron beam melted Ti-6Al-4V alloy, *Mater. Sci. Eng. A.* 744 (2019) 182–194. <https://doi.org/10.1016/j.msea.2018.12.016>.
- [31] C.L.A. Leung, R. Tosi, E. Muzangaza, S. Nonni, P.J. Withers, P.D. Lee, Effect of preheating on the thermal, microstructural and mechanical properties of selective electron beam melted Ti-6Al-4V components, *Mater. Des.* 174 (2019). <https://doi.org/10.1016/j.matdes.2019.107792>.
- [32] W. Kan, B. Chen, C. Jin, H. Peng, J. Lin, Microstructure and mechanical properties of a high Nb-TiAl alloy fabricated by electron beam melting, *Mater. Des.* 160 (2018) 611–623. <https://doi.org/10.1016/j.matdes.2018.09.044>.
- [33] B. Gao, H. Peng, Y. Liang, J. Lin, B. Chen, Electron beam melted TiC/high Nb-TiAl nanocomposite: Microstructure and mechanical property, *Mater. Sci. Eng. A.* 811 (2021). <https://doi.org/10.1016/j.msea.2021.141059>.
- [34] A.T. Sutton, C.S. Kriewall, S. Karnati, M.C. Leu, J.W. Newkirk, Characterization of AISI 304L stainless steel powder recycled in the laser powder-bed fusion process, *Addit. Manuf.* 32 (2020) 100981. <https://doi.org/10.1016/j.addma.2019.100981>.
- [35] A.B. Spierings, M. Voegtlin, T. Bauer, K. Wegener, Powder flowability characterisation methodology for powder-bed-based metal additive manufacturing, *Prog. Addit. Manuf.* 1 (2016) 9–20. <https://doi.org/10.1007/s40964-015-0001-4>.
- [36] C. Dharmendra, R. Alaghmandfard, A. Hadadzadeh, B.S. Amirkhiz, M. Mohammadi, Influence of build orientation on small-scale properties of electron beam melted Ti-6Al-4V, *Mater. Lett.* 266 (2020) 126970. <https://doi.org/10.1016/j.matlet.2019.126970>.
- [37] M. Koike, P. Greer, K. Owen, G. Lilly, L.E. Murr, S.M. Gaytan, E. Martinez, T. Okabe, Evaluation of titanium alloys fabricated using rapid prototyping technologies-electron beam melting and laser beam melting, *Materials (Basel)*. 4 (2011) 1776–1792. <https://doi.org/10.3390/ma4101776>.
- [38] C. Leyens, M. Peters, *Titanium and Titanium Alloys*, 2003.
- [39] E. Baril, L.P. Lefebvre, Y. Thomas, Interstitial elements in titanium powder metallurgy: Sources and control, *Powder Metall.* 54 (2011) 183–186. <https://doi.org/10.1179/174329011X13045076771759>.
- [40] I.E. Anderson, E.M.H. White, R. Dehoff, Feedstock powder processing research needs

- for additive manufacturing development, *Curr. Opin. Solid State Mater. Sci.* 22 (2018) 8–15. <https://doi.org/10.1016/j.cossms.2018.01.002>.
- [41] G. Chen, S.Y. Zhao, P. Tan, J. Wang, C.S. Xiang, H.P. Tang, A comparative study of Ti-6Al-4V powders for additive manufacturing by gas atomization, plasma rotating electrode process and plasma atomization, *Powder Technol.* 333 (2018) 38–46. <https://doi.org/10.1016/j.powtec.2018.04.013>.
- [42] C. Meier, R. Weissbach, J. Weinberg, W.A. Wall, A. John Hart, Modeling and characterization of cohesion in fine metal powders with a focus on additive manufacturing process simulations, *Powder Technol.* 343 (2019) 855–866. <https://doi.org/10.1016/j.powtec.2018.11.072>.
- [43] G. Soundarapandiyam, R. Khan, C. Johnston, B. Chen, M. Fitzpatrick, Effect of postprocessing thermal treatments on electron-beam powder bed-fused Ti6Al4V, *Mater. Des. Process. Commun.* (2020) 1–8. <https://doi.org/10.1002/mdp2.168>.
- [44] C. Körner, Additive manufacturing of metallic components by selective electron beam melting - A review, *Int. Mater. Rev.* 61 (2016) 361–377. <https://doi.org/10.1080/09506608.2016.1176289>.
- [45] J. Haubrich, J. Gussone, P. Barriobero-Vila, P. Kürnsteiner, E.A. Jäggle, D. Raabe, N. Schell, G. Requena, The role of lattice defects, element partitioning and intrinsic heat effects on the microstructure in selective laser melted Ti-6Al-4V, *Acta Mater.* 167 (2019) 136–148. <https://doi.org/10.1016/j.actamat.2019.01.039>.
- [46] N. Shen, K. Chou, Numerical Thermal Analysis in Electron Beam Additive, *Proc. ASME 2012 Int. Manuf. Sci. Eng. Conf.* (2012) 774–784.
- [47] E. Landau, E. Tiferet, Y.I. Ganor, R.K. Ganeriwala, M.J. Matthews, D. Braun, M. Chonin, G. Ziskind, Thermal characterization of the build chamber in electron beam melting, *Addit. Manuf.* 36 (2020) 101535. <https://doi.org/10.1016/j.addma.2020.101535>.
- [48] K. Zhang, J. Mei, N. Wain, X. Wu, Effect of Hot-Isostatic-Pressing Parameters on the Microstructure and Properties of Powder Ti-6Al-4V Hot-Isostatically-Pressed Samples, *Metall. Mater. Trans. A.* 41 (2010) 1033–1045. <https://doi.org/10.1007/s11661-009-0149-y>.

- [49] A. Montelione, S. Ghods, R. Schur, C. Wisdom, D. Arola, M. Ramulu, Powder Reuse in Electron Beam Melting Additive Manufacturing of Ti6Al4V: Particle Microstructure, Oxygen Content and Mechanical Properties, *Addit. Manuf.* 35 (2020) 101216. <https://doi.org/10.1016/j.addma.2020.101216>.
- [50] M. Yan, M.S. Dargusch, T. Ebel, M. Qian, A transmission electron microscopy and three-dimensional atom probe study of the oxygen-induced fine microstructural features in as-sintered Ti-6Al-4V and their impacts on ductility, *Acta Mater.* 68 (2014) 196–206. <https://doi.org/10.1016/j.actamat.2014.01.015>.
- [51] C. Ledford, M. Tung, C. Rock, T. Horn, Real time monitoring of electron emissions during electron beam powder bed fusion for arbitrary geometries and toolpaths, *Addit. Manuf.* 34 (2020) 101365. <https://doi.org/10.1016/j.addma.2020.101365>.
- [52] A. Bin Anwar, Q.C. Pham, Study of the spatter distribution on the powder bed during selective laser melting, *Addit. Manuf.* 22 (2018) 86–97. <https://doi.org/10.1016/j.addma.2018.04.036>.
- [53] C. Wei, X. Ma, X. Yang, M. Zhou, C. Wang, Y. Zheng, W. Zhang, Z. Li, Microstructural and property evolution of Ti6Al4V powders with the number of usage in additive manufacturing by electron beam melting, *Mater. Lett.* 221 (2018) 111–114. <https://doi.org/10.1016/j.matlet.2018.03.124>.
- [54] J.M. Oh, B.G. Lee, S.W. Cho, S.W. Lee, G.S. Choi, J.W. Lim, Oxygen effects on the mechanical properties and lattice strain of Ti and Ti-6Al-4V, *Met. Mater. Int.* 17 (2011) 733–736. <https://doi.org/10.1007/s12540-011-1006-2>.
- [55] C. de Formanoir, S. Michotte, O. Rigo, L. Germain, S. Godet, Electron beam melted Ti-6Al-4V: Microstructure, texture and mechanical behavior of the as-built and heat-treated material, *Mater. Sci. Eng. A.* 652 (2016) 105–119. <https://doi.org/10.1016/j.msea.2015.11.052>.
- [56] Y. Kim, E. Kim, Y. Song, S. Ho, Y. Kwon, Microstructure and mechanical properties of hot isostatically pressed Ti – 6Al – 4V alloy, *J. Alloys Compd.* 603 (2014) 207–212. <https://doi.org/10.1016/j.jallcom.2014.03.022>.
- [57] A. Farid, A. Usman, S. Dyuti, M. Ehsan, C. Kaylie, M. Yahya, T. Ehsan, Study of powder recycling and its effect on printed parts during laser powder-bed fusion of 17-4

PH stainless steel, *Journal Mater. Process Tech.* 278 (2020) 116522.
<https://doi.org/10.1016/j.jmatprotec.2019.116522>.

- [58] H. Masuo, Y. Tanaka, S. Morokoshi, H. Yagura, T. Uchida, Y. Yamamoto, Y. Murakami, Influence of defects, surface roughness and HIP on the fatigue strength of Ti-6Al-4V manufactured by additive manufacturing, *Int. J. Fatigue.* 117 (2018) 163–179. <https://doi.org/10.1016/j.ijfatigue.2018.07.020>.

Journal Pre-proof

Author Contributions

Gowtham Soundarapandiyam: Conceptualization, Methodology, Investigation, Writing - Original Draft, Visualization. **Carol Johnston:** Supervision, Writing - review & editing, Resources, Project administration. **Raja H.U. Khan:** Supervision, Conceptualization, Investigation, Resources, Writing - review & editing, **Chu Lun Alex Leung:** XCT experiment and analysis, Writing - Review & Editing, **Peter D. Lee:** Resources, **Everth Hernandez-Nava:** Methodology- Specimen preparation, Resources, Writing- review & editing. **Bo Chen:** Supervision, Investigation, Data Curation, Writing - review & editing. **Michael E. Fitzpatrick:** Supervision, Conceptualization, Resources, Writing - review & editing, Funding acquisition.

Declaration of interests

The authors declare that they have no known competing financial interests or personal relationships that could have appeared to influence the work reported in this paper.

The authors declare the following financial interests/personal relationships which may be considered as potential competing interests:

Journal Pre-proof